Emergence of metal-semiconductor phase transition in MX_2 (M =Ni, Pd, Pt; X =S, Se, Te) moiré superlattices

Jie Li(李杰), Rui-Zi Zhang(张瑞梓), Jinbo Pan(潘金波), Ping Chen(陈平), and Shixuan Du(杜世萱)

Citation: Chin. Phys. B, 2025, 34 (**3**): 037302. DOI: 10.1088/1674-1056/ada7d9
Journal homepage: http://cpb.iphy.ac.cn; http://iopscience.iop.org/cpb

What follows is a list of articles you may be interested in

Orbital *XY* models in moiré superlattices

Yanqi Li(李彦琪), Yi-Jie Wang(王一杰), and Zhi-Da Song(宋志达)
Chin. Phys. B, 2025, 34 (**2**): 027303. DOI: 10.1088/1674-1056/ad9ffc

Moiré physics in two-dimensional materials: Novel quantum phases and electronic properties

Zi-Yi Tian(田子弈), Si-Yu Li(李思宇), Hai-Tao Zhou(周海涛), Yu-Hang Jiang(姜宇航), and Jin-Hai Mao(毛金海)
Chin. Phys. B, 2025, 34 (**2**): 027301. DOI: 10.1088/1674-1056/ad9e96

$GaInX_3$ (X = S, Se, Te): Ultra-low thermal conductivity and excellent thermoelectric performance

Zhi-Fu Duan(段志福), Chang-Hao Ding(丁长浩), Zhong-Ke Ding(丁中科), Wei-Hua Xiao(肖威华), Fang Xie(谢芳), Nan-Nan Luo(罗南南), Jiang Zeng(曾犟), Li-Ming Tang(唐黎明), and Ke-Qiu Chen(陈克求)
Chin. Phys. B, 2024, 33 (**8**): 087302. DOI: 10.1088/1674-1056/ad47e3

Intrinsic valley-polarized quantum anomalous Hall effect in a two-dimensional germanene/MnI_2 van der Waals heterostructure

Xiao-Jing Dong(董晓晶) and Chang-Wen Zhang(张昌文)
Chin. Phys. B, 2024, 33 (**7**): 077303. DOI: 10.1088/1674-1056/ad4bbd

Effect of strain on structure and electronic properties of monolayer C_4N_4

Hao Chen(陈昊), Ying Xu(徐瑛), Jia-Shi Zhao(赵家石), and Dan Zhou(周丹)
Chin. Phys. B, 2024, 33 (**5**): 057302. DOI: 10.1088/1674-1056/ad260c

---

SPECIAL TOPIC — Moiré physics in two-dimensional materials

Emergence of metal–semiconductor phase transition in MX_2 (M = Ni, Pd, Pt; X = S, Se, Te) moiré superlattices

Jie Li(李杰)[1,†], Rui-Zi Zhang(张瑞梓)[2,†], Jinbo Pan(潘金波)[2,3], Ping Chen(陈平)[1,‡], and Shixuan Du(杜世萱)[2,3,4,§]

[1] *Center On Nanoenergy Research, Guangxi Key Laboratory for Relativistic Astrophysics, School of Physical Science and Technology, Guangxi University, Nanning* 530004, *China*

[2] *Beijing National Laboratory for Condensed Matter Physics, Institute of Physics, Chinese Academy of Sciences, Beijing* 100190, *China*

[3] *University of Chinese Academy of Sciences, Beijing* 100049, *China*

[4] *Songshan Lake Materials Laboratory, Dongguan* 523808, *China*

(Received 17 October 2024; revised manuscript received 13 December 2024; accepted manuscript online 9 January 2025)

Two-dimensional (2D) moiré superlattices with a small twist in orientation exhibit a broad range of physical properties due to the complicated intralayer and interlayer interactions modulated by the twist angle. Here, we report a metal–semiconductor phase transition in homojunction moiré superlattices of NiS_2 and $PtTe_2$ with large twist angles based on high-throughput screening of 2D materials MX_2 (M = Ni, Pd, Pt; X = S, Se, Te) via density functional theory (DFT) calculations. Firstly, the calculations for different stacking configurations (AA, AB and AC) reveal that AA stacking ones are stable for all the bilayer MX_2. The metallic or semiconducting properties of these 2D materials remain invariable for different stacking without twisting except for NiS_2 and $PtTe_2$. For the twisted configurations, NiS_2 transfers from metal to semiconductor when the twist angles are 21.79°, 27.79°, 32.20° and 60°. $PtTe_2$ exhibits a similar transition at 60°. The phase transition is due to the weakened d–p orbital hybridization around the Fermi level as the interlayer distance increases in the twisted configurations. Further calculations of untwisted bilayers with increasing interlayer distance demonstrate that all the materials undergo metal–semiconductor phase transition with the increased interlayer distance because of the weakened d–p orbital hybridization. These findings provide fundamental insights into tuning the electronic properties of moiré superlattices with large twist angles.

Keywords: moiré superlattices, first-principles calculations, metal–semiconductor phase transition

PACS: 73.21.Cd, 71.15.Mb, 71.30.+h

DOI: 10.1088/1674-1056/ada7d9 **CSTR:** 32038.14.CPB.ada7d9

1. Introduction

Twisted graphene systems have emerged as a pivotal platform for studying correlated phenomena in condensed matter physics, strange phase encompassing unconventional superconductivity,[1–3] correlated insulators,[4–6] orbital magnets,[7–9] quantum Hall states[10,11] and strange metals.[12] These exotic phases originate from electron–electron interactions within the moiré flat bands.[13] Similar to graphene, bilayer transition metal dichalcogenides (TMDs) have also attracted significant interest due to the emergence of moiré flat bands.[14] The moiré flat bands in TMDs persist over a wide range of twist angles.[15] Additionally, the diversity of TMD materials facilitates the formation of both homo- and heterojunctions, further enriching the study of correlated phenomena, including Wigner crystal states,[16] correlated phases,[17] the Hubbard model[18,19] and other intriguing physical phenomena.

Previous research primarily focused on the strongly correlated phenomena in moiré flat bands induced by magic twist angles. At larger twist angles (nearly 30°), TMD materials, such as MoS_2, $MoSe_2$, WS_2 and WSe_2, exhibited weaker correlated behavior.[20,21] Some studies have reported that materials such as $PtSe_2$, PtS_2 and $PtTe_2$ exhibit flat bands even at relatively large twist angles, with the band edges primarily dominated by p_z orbitals or d_z^2 orbitals from the outermost atoms.[22,23] The flat bands arise from significant hybridization between adjacent atomic orbitals, which strengthens interlayer interactions beyond simple van der Waals (VDW) forces.[24] Even when the bands become dispersive at large twist angles, it remains valuable to investigate whether MX_2 materials, where the band edges are predominantly composed of p_z orbitals,[25–31] could give rise to new physical phenomena.

In this paper, we report a metal–semiconductor phase transition in NiS_2 and $PtTe_2$ moiré superlattices at large twist angles. We started from the stacking properties of MX_2 materials and found the stable stacking (AA stacking) via DFT

†These authors contributed equally to this work.

‡Corresponding author. E-mail: chenping@gxu.edu.cn

§Corresponding author. E-mail: sxdu@iphy.ac.cn

calculations. We found that NiS_2 and $PtTe_2$ exhibit metallic or semiconducting behavior depending on their stacking configuration. We then constructed twisted structures at large twist angles and found that phase transitions from a metal to a semiconductor happened in NiS_2 and $PtTe_2$. NiS_2 undergoes a phase transition at 21.79°, 27.79°, 32.20° and 60°, while $PtTe_2$ shows a phase transition at 60°. When the material phase transitions happen, structural misalignment occurs. In addition, the projected density of states (PDOS) reveals that the hybridized d–p orbital weakens. The unfolded band structures further demonstrate that the d–p orbital hybridization weakens and the band structure changes with twist. This suggests that twist influences both interlayer and intralayer interactions. According to the calculations of the bilayer untwisted configurations, we find that the interlayer distance variation coming from the AA, AB and AC stacking configurations could influence the electronic structures significantly. To identify the most critical factor driving the phase transition, we calculated 36 band structures in untwisted configurations with fixed interlayer distances. The results show that while the band shape remains unchanged, the band gap opens and increases as the interlayer distance increases. This indicates that the primary mechanism of the phase transition is the weakening hybridization of the d–p orbital with the change of interlayer spacing induced by the twist.

2. Calculation methods

2.1. DFT calculation methods

All structural optimizations were performed using the Vienna *Ab initio* Simulation Package (VASP).[32,33] The projected augmented wave (PAW) method was applied with pseudopotentials.[34] The Perdew–Burke–Ernzerhof (PBE) exchange–correlation functional was employed.[35] To account for VDW interactions, we employed Grimme's DFT-D3 method with a zero-damping function.[36] A vacuum layer of 20 Å was introduced for all structures to avoid interlayer interactions. For geometric optimization, the force criterion for each atom was set to less than 10^{-2} eV·Å^{-1}, while the energy convergence criterion was 10^{-6} eV. The PAW cutoff energy was set to 500 eV, and a Gamma-centered k-point mesh was used for Brillouin zone sampling. Orbital-projected band structures were obtained using the VASPKIT software.[37]

2.2. Moiré superlattice build-up methods.

For constructing moiré superlattices, the configurations were generated from individual monolayers.[38,39] In the primitive cell of a single layer, $\boldsymbol{a}_1$ and $\boldsymbol{a}_2$ represent the lattice vectors, which form an angle of 120° between them. To ensure that the two twisted layers have the same size and align properly, we need to identify integer pairs (M, N) that satisfy the following conditions:

$$|M\boldsymbol{a}_1 + N\boldsymbol{a}_2| = |M'\boldsymbol{a}_1 + N'\boldsymbol{a}_2|. \tag{1}$$

As shown in supporting material Fig. S1, the four vectors defining the two-layer materials are selected as follows:

$$\boldsymbol{V}_1 = (M+N)\,\boldsymbol{a}_1 + M\boldsymbol{a}_2, \tag{2}$$

$$\boldsymbol{V}_2 = -M\boldsymbol{a}_1 + N\boldsymbol{a}_2, \tag{3}$$

$$\boldsymbol{V}_1' = (M+N)\,\boldsymbol{a}_1 + N\boldsymbol{a}_2, \tag{4}$$

$$\boldsymbol{V}_2' = -N\boldsymbol{a}_1 + M\boldsymbol{a}_2, \tag{5}$$

where $\boldsymbol{V}_1$ and $\boldsymbol{V}_2$ are the lattice parameters of the top layer, while $\boldsymbol{V}_1'$ and $\boldsymbol{V}_2'$ are the lattice parameters of the bottom layer.

The corresponding lengths of these vectors are

$$B^2 = a^2\left(M^2 + MN + N^2\right). \tag{6}$$

The relative length between $\boldsymbol{V}_1$ ($\boldsymbol{V}_2$) and $\boldsymbol{V}_1'$ ($\boldsymbol{V}_2'$) of the two layers is expressed as

$$C^2 = (M-N)^2 a^2. \tag{7}$$

The twist angle between the two layers can be obtained using the following formula:

$$B^2 + B^2 - 2B^2\cos\theta = C^2. \tag{8}$$

Thus

$$\theta = \arccos\frac{M^2 + 4NM + N^2}{2\left(M^2 + NM + N^2\right)}. \tag{9}$$

In summary, the transformation matrix for constructing the moiré superlattices between the two layers is

$$\boldsymbol{T}_1 = \begin{pmatrix} M+N & M & 0 \\ -M & N & 0 \\ 0 & 0 & 1 \end{pmatrix}, \tag{10}$$

$$\boldsymbol{T}_2 = \begin{pmatrix} M+N & N & 0 \\ -N & M & 0 \\ 0 & 0 & 1 \end{pmatrix}. \tag{11}$$

To achieve additional twisted angles, the bottom or top layer can be rotated by 180°, which can also be accomplished by multiplying the transformation matrix

$$\boldsymbol{T}_3 = \begin{pmatrix} -1 & 0 & 0 \\ 0 & -1 & 0 \\ 0 & 0 & 1 \end{pmatrix}. \tag{12}$$

Moreover, due to the threefold rotational symmetry of TMDs, the twisted configuration at 0° is equivalent to that at 120°.

3. Results and discussion

In moiré superlattices, the local stacking order is crucial for understanding their electronic structure.[40,41] We explored three different stacking configurations, AA, AB and AC, as illustrated in Fig. 1(a). By designating the M atom in the top layer as a reference point, we noted the following alignments:

in AA stacking, the top layer M atom aligns with the M atom in the bottom layer; in AB stacking, the top layer M atom aligns with the bottom X atom of the bottom layer; and in AC stacking, the top layer M atom aligns with the top X atom of the bottom layer. These different stacking configurations alter the relative distances between the outer layers, potentially leading to changes in the electronic structure.

The binding energies of different stacking configurations are illustrated in Fig. 1(b). The binding energies are defined as $E_b = E_{\text{homojunction}} - 2 \times E_{\text{monolayer}}$. AA stacking consistently represents the most stable structure, exhibiting the lowest energy among MX_2 configurations. In contrast, AB and AC stacking configurations are higher in energy, ranging from approximately 10 meV to 50 meV. For comparison, the energy difference for graphene is around 4 meV,[42] while for MoS_2 it is about 10 meV.[43] These findings indicate that AB and AC stacking are unstable, suggesting that these configurations are challenging to synthesize.

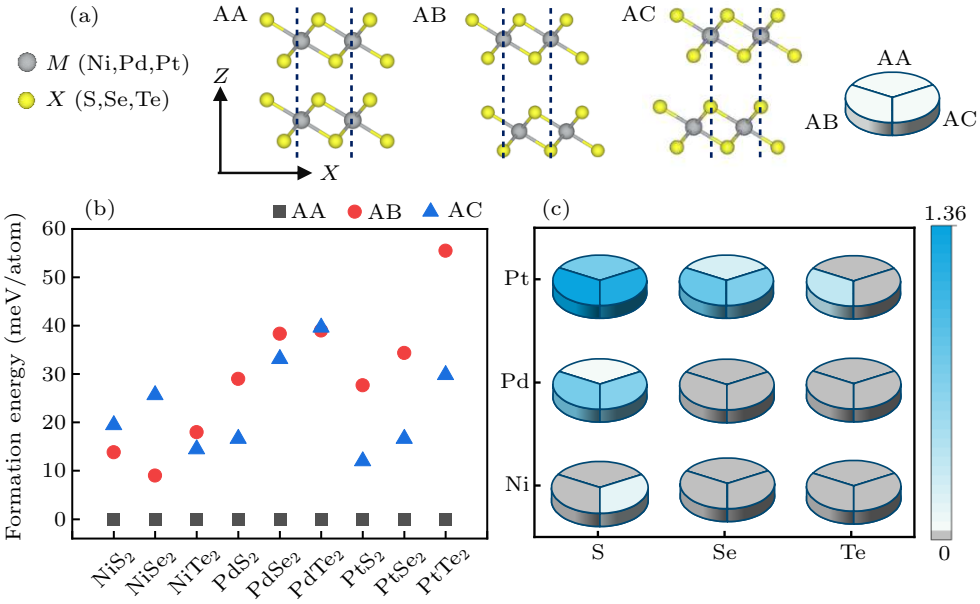

Fig. 1. Crystal structure, binding energy and band gap properties. (a) Side view of AA, AB and AC stacking configurations. (b) Binding energy of each stacking configuration, with AA stacking set as the reference (0 eV). (c) Band gap of different stacking configurations, depicted in pie charts: top for AA, left for AB and right for AC. The color bar indicates the band gap value, with gray representing metallic states.

We calculated the electronic properties of MX_2 materials, with their band gaps illustrated in the pie chart of Fig. 1(c). The metallic nature of these materials is enhanced from S and Se to Te and from Pt and Pd to Ni, as the band gap decreases. This feature corresponds to the monolayer band structures shown in the supporting material (Figs. S2 and S3). Notably, PtS_2, PdS_2 and $PtSe_2$ consistently exhibit semiconducting features, while $PdSe_2$, $NiSe_2$, $PdTe_2$ and $NiTe_2$ exhibit metallic features. Interestingly, NiS_2 and $PtTe_2$ both exhibit semiconductor and metallic characteristics at different stacking configurations: NiS_2 has a band gap of 0 eV at AA stacking and AB stacking, and 0.13 eV at AC stacking, while $PtTe_2$ has a band gap of 0 eV at AA stacking and AC stacking, and 0.33 eV at AB stacking. All the band structures are plotted in supporting material Fig. S4. These results reveal that their electronic structures are sensitive to the relative positions of the two layers.

We studied the band structure of moiré superlattices by selecting NiS_2 and $PtTe_2$ due to their differing electronic behaviors at various stacking configurations. The results for specific angles of 13.17°, 21.79° and 32.20° are illustrated in Figs. 2(a), 2(b) and 2(c). Each twisted structure comprises three distinct stacking configurations, denoted by three colors: purple for AA, blue for AB and green for AC. Variations in the twist angle alter the relative spatial distributions of these stacking arrangements. Using NiS_2 as an example, we established the relationship between the twist angle and the parameters of the moiré superlattices, as illustrated in Fig. 2(d). Certain twist angles result in larger moiré supercells containing more atoms. Therefore, we focus on relatively smaller supercells corresponding to larger twist angles: 0°, 13.17°, 21.79°, 27.79°, 32.20°, 38.21°, 46.83° and 60°. The band gaps for these configurations, calculated without considering spin–orbit coupling (SOC), are presented in Fig. 2(e). For NiS_2, band gaps are observed at 21.79° (0.12 eV), 27.79° (0.15 eV), 32.20° (0.13 eV) and 60° (0.33 eV), while at other twist angles it exhibits as a metal with a zero band gap. In contrast, $PtTe_2$ only exhibits semiconducting features at 60°, with a band gap of 0.39 eV; it exhibits as a metal at other twist angles. The variation in twist angle induces a metal–semiconductor phase transition in both materials. It is noteworthy that the bands do not become remarkably flat at these twist angles (see supporting material Fig. S5). We also investigate the effect of SOC, as shown in supporting material Fig. S6. The SOC effect leads

to splits of the band around the Fermi level and changes the band gap, especially for $PdTe_2$. The semiconductor band gap of NiS_2 changes by less than 10 meV, while for $PtTe_2$ the band gap shifts by 290 meV. However, the SOC did not affect the metal–semiconductor phase transition results. According to the density of states (DOS) (see supporting material Fig. S7), the valance band is dominated by p-orbitals when transitioning from metal to semiconductor and the semiconductor properties are similar to the monolayer, as shown in the monolayer DOS (see supporting material Fig. S8).

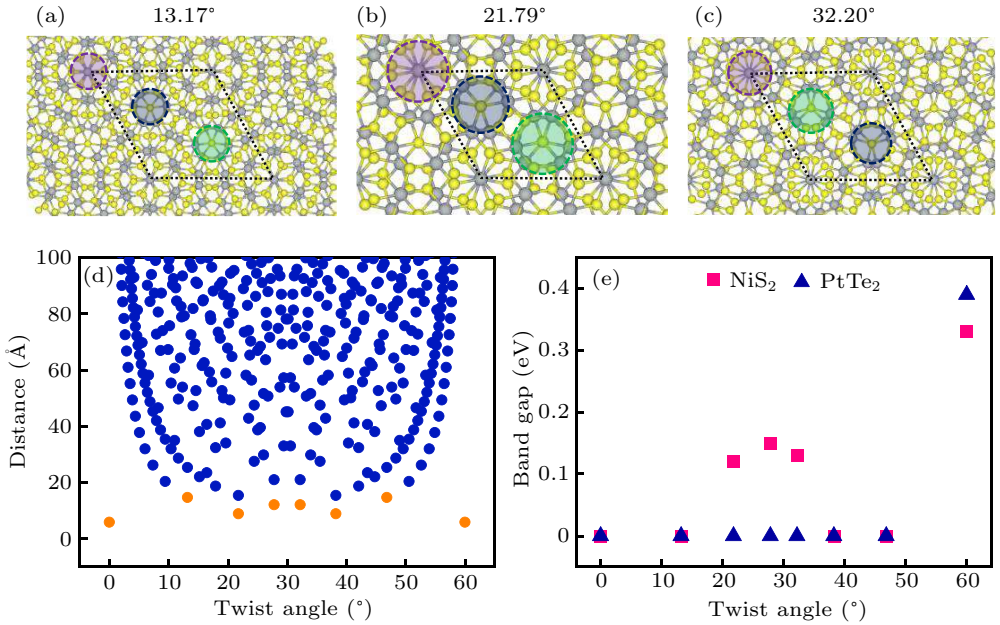

Fig. 2. Crystal structure, moiré lattice parameters and band gap values at different twist angles. (a)–(c) Top view of the twisted homojunction at 13.17°, 21.79° and 32.20°, with the moiré superlattices unit cell marked in black. (d) Moiré superlattices constant as a function of twist angle for NiS_2. (e) Computed band gaps of NiS_2 and $PtTe_2$ versus twist angle.

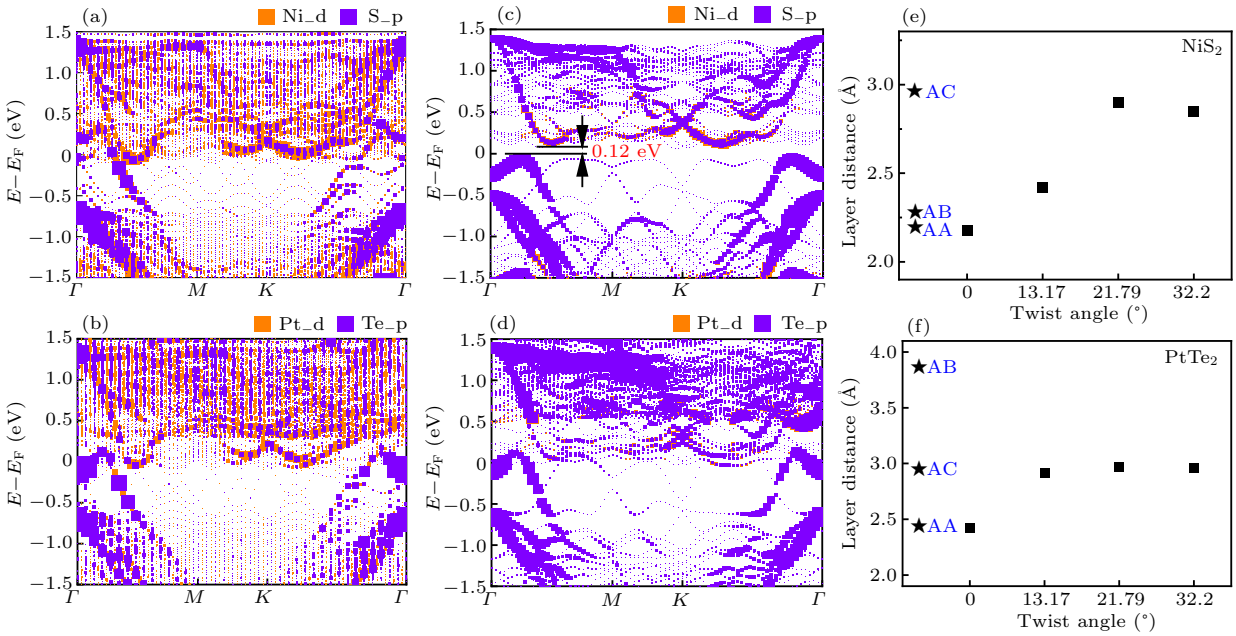

Fig. 3. Computed atomic orbital-projected effective band structures (PEBS) of NiS_2 and $PtTe_2$: (a) and (c) PEBS of NiS_2 at 13.17° and 21.79°. (b) and (d) PEBS of $PtTe_2$ at 13.17° and 21.79°. (e), (f) Interlayer distance versus twist angle for NiS_2 and $PtTe_2$, with the interlayer distances of the AA, AB and AC crystal structures indicated by pentagrams.

We further studied the unfolded band structures projected onto the atomic orbitals of NiS_2 and $PtTe_2$. For NiS_2, as the twist angle changes from 13.17° to 21.79°, as shown in Figs. 3(a) and 3(c), the Fermi level at a twist angle of 13.17° is predominantly composed of Ni d and S p orbitals. As the twist angle increases to 21.79°, the valence band maximum is primarily determined by S p orbitals. This transition suggests a reduced hybridization between the d and p orbitals, leading to the opening of a band gap of 0.12 eV. Figures 3(b) and 3(d) present the unfolded band structure of $PtTe_2$; at both

13.17° and 21.79°, the Fermi level is predominantly composed of Pt d orbitals and Te p orbitals. Furthermore, a significant change in the shape of the conduction band minimum is observed between 13.17° and 21.79°, as well as between 38.21° and 46.83°, for both NiS_2 and $PtTe_2$ (see supporting material Fig. S9). This suggests that the twist angle influences interlayer interactions, with the phase transition occurring as a result of the weakened d–p orbital hybridization.

The weakened d–p orbital hybridization should be related to the interlayer interaction. Hence, we investigate the interlayer distances of NiS_2 and $PtTe_2$ at different twist angles, as shown in Figs. 3(e) and 3(f). Due to structural optimization, the twisted structures underwent deformation, and the interlayer distance was defined as the average distance between the central atoms of the bilayer materials. The interlayer distances for all twisted structures fall within the range of those in the AA, AB and AC stacking configurations. For twisted NiS_2, the interlayer distance ranges from 2.42 Å to 2.85 Å, within the 2.18 Å to 2.95 Å range for the stacking configurations. For twisted $PtTe_2$, the interlayer distance ranges from 2.92 Å to 2.97 Å, within the 2.42 Å to 3.84 Å range for the stacking configurations. Hence, the interlayer distance affects d–p orbital hybridization, further inducing the phase transition.

To understand the mechanism of the phase transition, we calculated the band structures of the three stacking configurations at different interlayer distances. For each material, specific interlayer distances were selected for the AA, AB and AC configurations, with six evenly spaced points chosen. The band structures were computed at fixed interlayer distances without structural optimization. It was found that each stacking configuration can undergo a metal–semiconductor phase transition, as shown in Figs. 4(a) and 4(b). The band gap increases with the interlayer distance and tends to indicate semiconductor behavior. Conversely, smaller distances lean toward metallic characteristics. For NiS_2, the metal–semiconductor phase transition for AA and AC stacking occurs at an interlayer distance of 2.86 Å, while for AB stacking it occurs at 3.32 Å. For $PtTe_2$, the phase transition interlayer distances are 3.27 Å for AA and AC stacking and 3.56 Å for AB stacking.

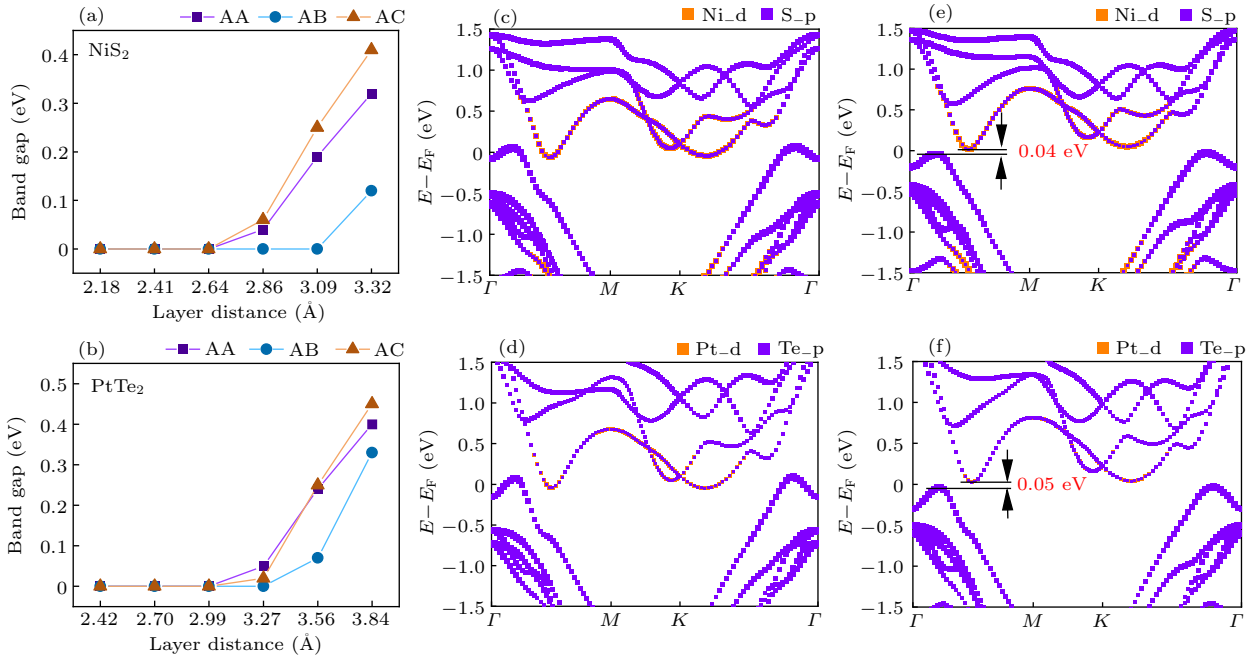

Fig. 4. The band gap values of different stacking configurations and atomic orbital projected band structure (PBAND). (a), (b) Computed band gap values for three stacking configurations of NiS_2 and $PtTe_2$. (c), (e) PBAND of NiS_2 with AA stacking at interlayer distances of 2.64 Å and 2.86 Å. (d), (f) PBAND of $PtTe_2$ with AA stacking at interlayer distances of 2.99 Å and 3.27 Å.

Furthermore, we plotted the atomic orbital-projected band structures of NiS_2 for AA stacking at interlayer distances of 2.64 Å and 2.86 Å, as shown in Figs. 4(c) and 4(e). Notably, as the interlayer distance increases, the separation between the conduction band and the valence band also increases, gradually opening a band gap of 0.04 eV. In Figs. 4(d) and 4(f), $PtTe_2$ exhibits a phase transition trend similar to that of NiS_2, with a band gap opening of 0.05 eV as the interlayer distance increases from 2.99 Å to 3.27 Å. Additional calculations for other interlayer distances and stacking configurations are shown in the supporting material (Fig. S10), where all band structures maintain their shape as the interlayer distance increases. And the weakened d–p orbital hybridization is induced by the change in interlayer distance. We also calculated the binding energy around the equilibrium interlayer distance (see supporting material Fig. S11). The binding energy is higher than this value, indicating that twisting can lead to structures with interlayer distances that cannot form in reality.

The interlayer distance governs the extent of d–p orbital hybridization, thereby driving the phase transition. As the interlayer distance increases, d–p orbital hybridization weakens, reducing interlayer interactions and causing the moiré superlattices to exhibit single-layer semiconductor properties. Conversely, a decrease in interlayer distance enhances d–p orbital hybridization, strengthening interlayer interactions and inducing metallic behavior. The moiré superlattices provide an accessible approach to control the interlayer distance and further manipulate phase transitions. On the one hand, the twist angle serves as a novel method for electronic tuning, facilitating transitions between high- and low-resistance states corresponding to the metal–insulator phase change, thereby enabling device switching. On the other hand, the uneven moiré potential modulation induced by the stacking twist enables selective tuning of the transport region,[44] which could potentially enhance the performance of logic, sensing and detection devices.

4. Conclusion

In summary, we found that the bilayers of NiS_2 and $PtTe_2$ exhibit a metal–semiconductor transition at different twist angles. Among all the MX_2 materials, AA stacking is the most stable configuration. Unlike other MX_2 materials, both NiS_2 and $PtTe_2$ demonstrate metallic and semiconductor characteristics depending on their stacking configurations. After calculating the DOS for the moiré superlattices, we observed a weakening of the hybridized d–p orbital following the metal–semiconductor transition. We observed that the interlayer distances in the twisted structures differ significantly from those in the AA, AB and AC stacking configurations. The unfolded band structure further reveals a weakening of d–p orbital hybridization, which we propose as the primary mechanism driving the phase transition. To verify this mechanism, we calculated 36 band structures at various fixed interlayer distances. We observed that the materials undergo a phase transition at different distances while preserving their band shapes, with weakened d–p orbital hybridization during the transition. This suggests that the moiré superlattices primarily influence the extent of d–p orbital hybridization. Our research provides insights into moiré superlattices as a transformative approach for manipulating electronic structures.

Acknowledgements

Project supported by the National Natural Science Foundation of China (Grant Nos. 52472153, 11704081, and 62488201), the National Key Research and Development Program of China (Grant No. 2022YFA1204100), National Science and Technology Innovation Talent Cultivation Program (Grant No. 2023BZRC016), Guangxi Natural Science Foundation (Grant No. 2020GXNSFAA297182), and the special fund for "Guangxi Bagui Scholars."

References

[1] Stepanov P, Das I, Lu X B, Fahimniya A, Watanabe K, Taniguchi T, Koppens F H L, Lischner J, Levitov L and Efetov D K 2020 *Nature* **583** 375
[2] Cao Y, Fatemi V, Fang S, Watanabe K, Taniguchi T, Kaxiras E and Jarillo-Herrero P 2018 *Nature* **556** 43
[3] Saito Y, Ge J Y, Watanabe K, Taniguchi T and Young A F 2020 *Nat. Phys.* **16** 926
[4] Cao Y, Fatemi V, Demir A, Fang S, Tomarken S L, Luo J Y, Sanchez-Yamagishi J D, Watanabe K, Taniguchi T, Kaxiras E, Ashoori R C and Jarillo-Herrero P 2018 *Nature* **556** 80
[5] Shen C, Chu Y B, Wu Q S, Li N, Wang S P, Zhao Y C, Tang J, Liu J Y, Tian J P, Watanabe K, Taniguchi T, Yang R, Meng Z Y, Shi D X, Yazyev O V and Zhang G Y 2020 *Nat. Phys.* **16** 520
[6] Liu X M, Hao Z Y, Khalaf E, Lee J Y, Ronen Y, Yoo H, Najafabadi D H, Watanabe K, Taniguchi T, Vishwanath A and Kim P 2020 *Nature* **583** 221
[7] Sharpe A L, Fox E J, Barnard A W, Finney J, Watanabe K, Taniguchi T, Kastner M A and Goldhaber-Gordon D 2019 *Science* **365** 605
[8] Lin J X, Zhang Y H, Morissette E, Wang Z, Liu S, Rhodes D, Watanabe K, Taniguchi T, Hone J and Li J I A 2022 *Science* **375** 437
[9] Lu X B, Stepanov P, Yang W, Xie M, Aamir M A, Das I, Urgell C, Watanabe K, Taniguchi T, Zhang G Y, Bachtold A, MacDonald A H and Efetov D K 2019 *Nature* **574** 653
[10] Serlin M, Tschirhart C L, Polshyn H, Zhang Y, Zhu J, Watanabe K, Taniguchi T, Balents L and Young A F 2020 *Science* **367** 900
[11] Kim D, Kang B, Choi Y B, Watanabe K, Taniguchi T, Lee G H, Cho G Y and Kim Y 2023 *Nano Lett.* **23** 163
[12] Cao Y, Chowdhury D, Rodan-Legrain D, Rubies-Bigorda O, Watanabe K, Taniguchi T, Senthil T and Jarillo-Herrero P 2020 *Phys. Rev. Lett.* **124** 076801
[13] Mak K F and Shan J 2022 *Nat. Nanotechnol.* **17** 686
[14] Angeli M and MacDonald A H 2021 *Proc. Natl. Acad. Sci. USA* **118** e2021826118
[15] Zhang Z M, Wang Y M, Watanabe K, Taniguchi T, Ueno K, Tutuc E and LeRoy B J 2020 *Nat. Phys.* **16** 1093
[16] Regan E C, Wang D Q, Jin C H, Utama M I, Gao B N, Wei X, Zhao S H, Zhao W Y, Zhang Z C, Yumigeta K, Blei M, Carlstrom J D, Watanabe K, Taniguchi T, Tongay S, Crommie M, Zettl A and Wang F 2020 *Nature* **579** 359
[17] Wang L, Shih E M, Ghiotto A, Xian L, Rhodes D A, Tan C, Claassen M, Kennes D M, Bai Y S, Kim B, Watanabe K, Taniguchi T, Zhu X Y, Hone J, Rubio A, Pasupathy A N and Dean C R 2020 *Nat. Mater.* **19** 861
[18] Tang Y H, Li L Z, Li T X, Xu Y, Liu S, Barmak K, Watanabe K, Taniguchi T, MacDonald A H, Shan J and Mak K F 2020 *Nature* **579** 353
[19] Xu Y, Kang K F, Watanabe K, Taniguchi T, Mak K F and Shan J 2022 *Nat. Nanotechnol.* **17** 934
[20] Constantinescu G C and Hine N D M 2015 *Phys. Rev. B* **91** 195416
[21] Lu N, Guo H Y, Zhuo Z W, Wang L, Wu X J and Zeng X C 2017 *Nanoscale* **9** 19131
[22] Klebl L, Xu Q, Fischer A, Xian L, Claassen M, Rubio A and Kennes D M 2022 *Electron. Struct.* **4** 014004
[23] Xu Q L, Guo Y Z and Xian L D 2022 *2D Mater.* **9** 014005
[24] Ahn J, Kang S H, Yoon M and Krogel J T 2024 *Phys. Rev. Res.* **6** 033177
[25] Lin M K, Villaos R A B, Hlevyack J A, Chen P, Liu R Y, Hsu C H, Avila J, Mo S K, Chuang F C and Chiang T C 2020 *Phys. Rev. Lett.* **124** 036402
[26] Ghasemi F, Taghavimendi R and Bakhshayeshi A 2020 *Opt. Quantum Electron.* **52** 492
[27] Jakhar M, Singh J, Kumar A and Pandey R 2020 *J. Phys. Chem. C* **124** 26565

[28] Zhang L, Yang T, Arramel, Feng Y P, Wee A T S and Wang Z 2022 *Nanoscale* **14** 7650
[29] Ahmad S 2017 *Mater. Chem. Phys.* **198** 162
[30] Mohammed H A H, Dongho-Nguimdo G M and Joubert D P 2019 *Mater. Today Commun.* **21** 100661
[31] Liu C, Lian C S, Liao M H, Wang Y, Zhong Y, Ding C, Li W, Song C L, He K, Ma X C, Duan W H, Zhang D, Xu Y, Wang L L and Xue Q K 2018 *Phys. Rev. Mater.* **2** 094001
[32] Kresse G and Furthmuller J 1996 *Comput. Mater. Sci.* **6** 15
[33] Kresse G and Furthmuller J 1996 *Phys. Rev. B* **54** 11169
[34] Blochl P E 1994 *Phys. Rev. B* **50** 17953
[35] Perdew J P, Burke K and Ernzerhof M 1998 *Phys. Rev. Lett.* **80** 891
[36] Grimme S, Antony J, Ehrlich S and Krieg H 2010 *J. Chem. Phys.* **132** 154104
[37] Wang V, Xu N, Liu J C, Tang G and Geng W T 2021 *Comput. Phys. Commun.* **267** 108033
[38] Carr S, Fang S and Kaxiras E 2020 *Nat. Rev. Mater.* **5** 748
[39] Song H Q, Liu Z and Zhang D B 2019 *Phys. Lett. A* **383** 2628
[40] Jung J, Raoux A, Qiao Z H and MacDonald A H 2014 *Phys. Rev. B* **89** 205414
[41] Naik M H and Jain M 2018 *Phys. Rev. Lett.* **121** 266401
[42] Wei T R, Jin M, Wang Y C, Chen H Y, Gao Z Q, Zhao K P, Qiu P F, Shan Z W, Jiang J, Li R B, Chen L D, He J and Shi X 2020 *Science* **369** 542
[43] Tao P, Guo H H, Yang T and Zhang Z D 2014 *Chin. Phys. B* **23** 106801
[44] Li X N, Lv Y W, Tong Q J, Liao L, Li K L and Jiang C Z 2023 *IEEE Electron Device Lett.* **44** 544